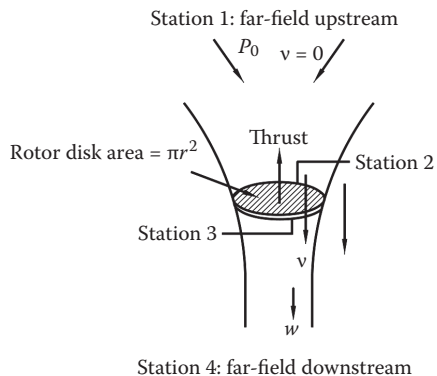Figure 2.1
Rotor disk and slip stream.

002x001.eps

Figure 2.2
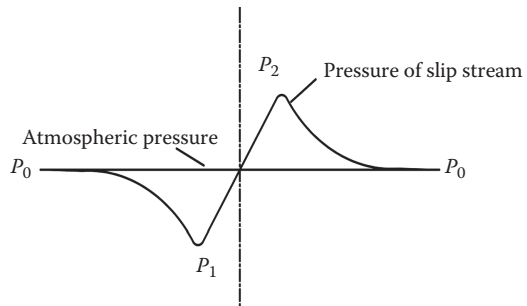Flow condition in the slip stream.
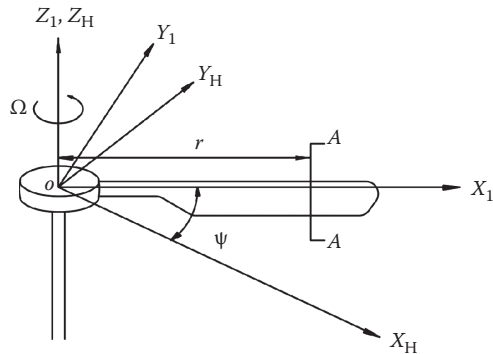
Figure 2.3
Pressure variation along the slip stream.

Figure 2.4
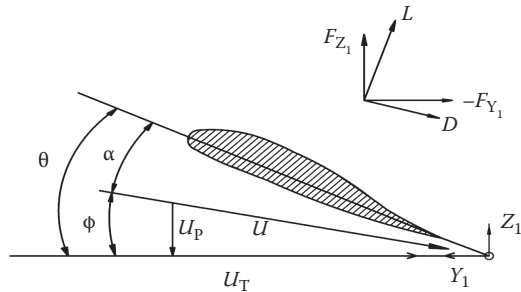Nonrotating hub fixed and rotating blade fixed coordinate systems.

Figure 2.5
Typical cross section of a rotor blade at radial location r and the velocity components.
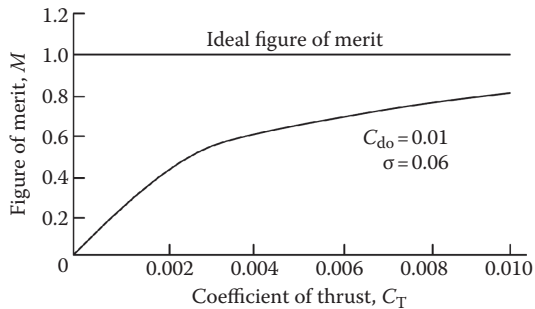
Figure 2.6
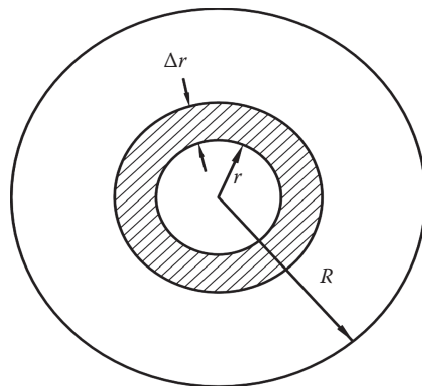Variation of figure of merit with thrust coefficient.

Figure 2.7
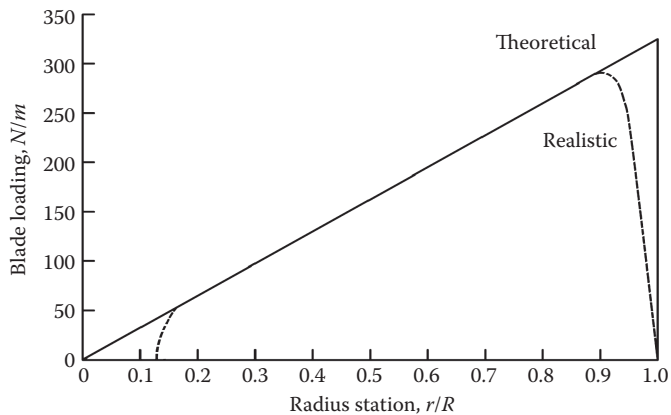Annular area for nonuniform inflow calculation.

Figure 2.8
Spanwise lift distribution on the blade, showing the tip and the root offset effects.
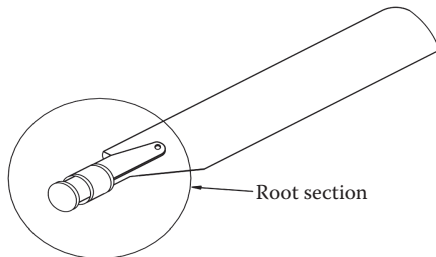
Figure 2.9
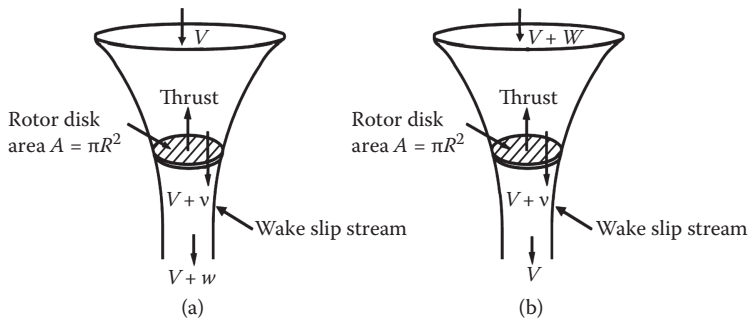Rotor blade root section/root cutout.

Figure 2.10
Flow velocities in climb and descent. (a) Climb ($V > 0$). (b) Descent ($V < 0$).
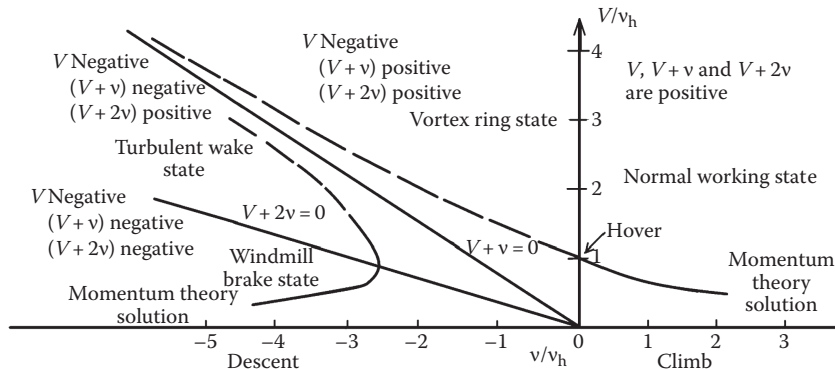
Figure 2.11
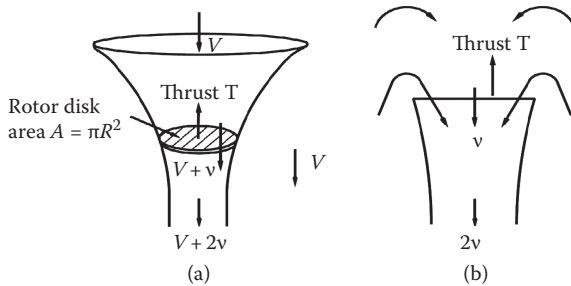Variation of induced flow as a function of climb and descent speed.

Figure 2.12
Flow pattern in the normal working state. (a) Climb ($V > 0$). (b) Hover ($V = 0$).
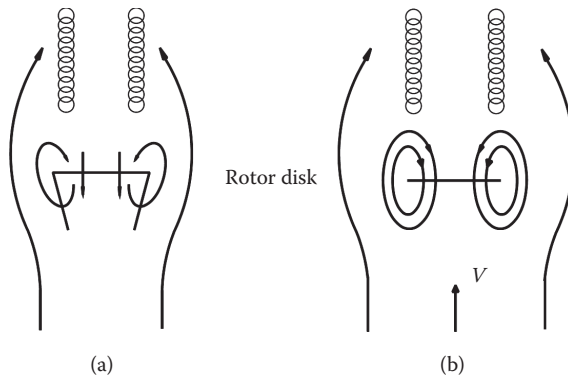
Figure 2.13
Flow pattern and velocities in the vortex ring state. (a) Low descent rates. (b) High descent rates.
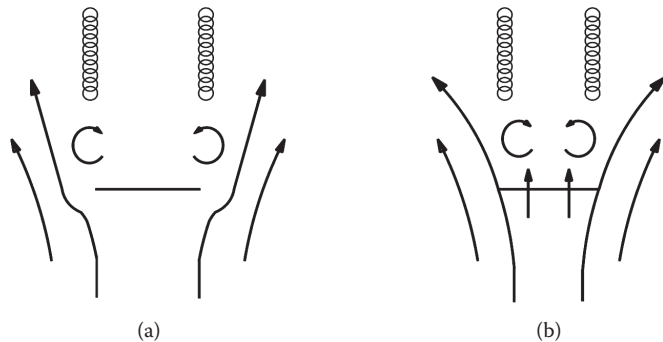
Figure 2.14
Flow pattern in the turbulent wake state. (a) Ideal autorotation ($V + v = 0$). (b) Tubulent wake state.
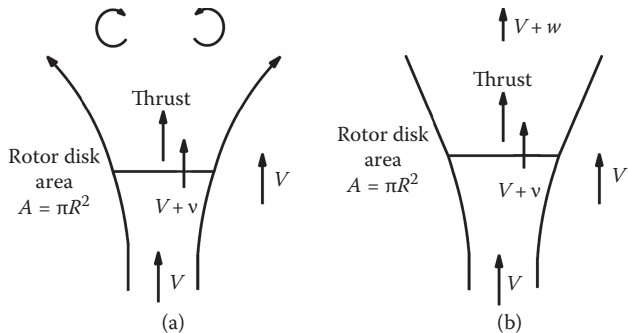
Figure 2.15
Flow pattern in the windmill brake state. (a) Boundary ($V + 2V = 0$). (b) Windmill brake state.
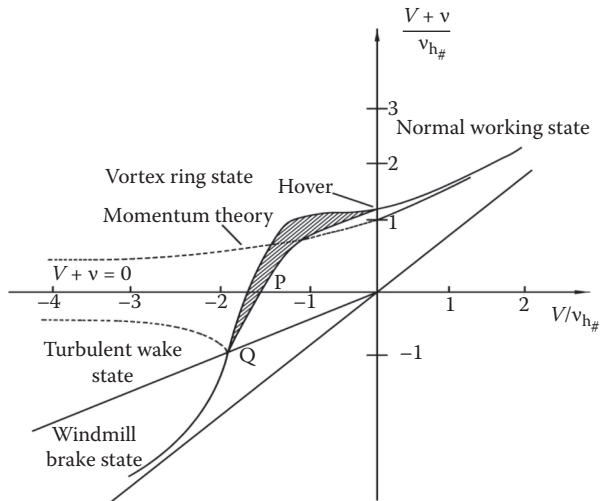
Figure 2.16
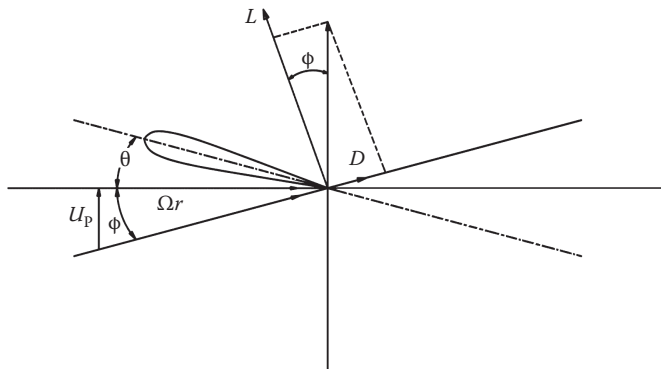Total inflow as a function of climb and descent speed.

Figure 2.17
Components of relative airflow and aerodynamic forces acting on a blade section during descent.
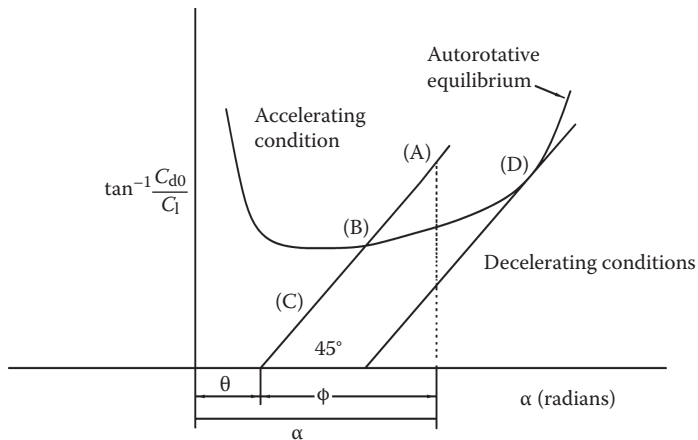
Figure 2.18
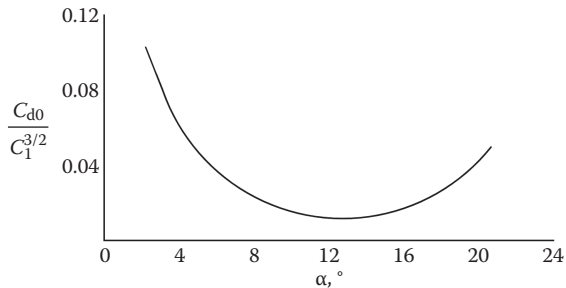Effect of operating pitch angle at autorotation condition.

Figure 2.19
Variation of $\dfrac{C_{d0}}{C_l^{3/2}}$ with an angle of attack for a typical airfoil.
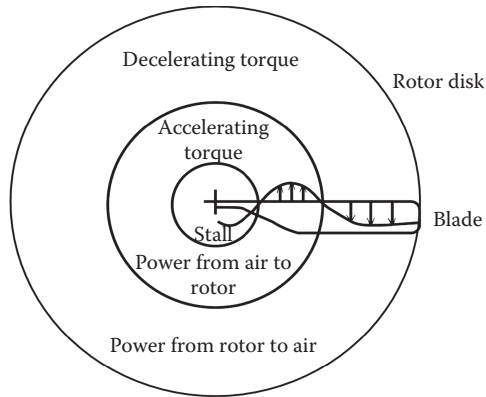
002x019.eps

Figure 2.20
Aerodynamic condition in terms of the in-plane sectional loads acting along the span of the blade during autorotation.
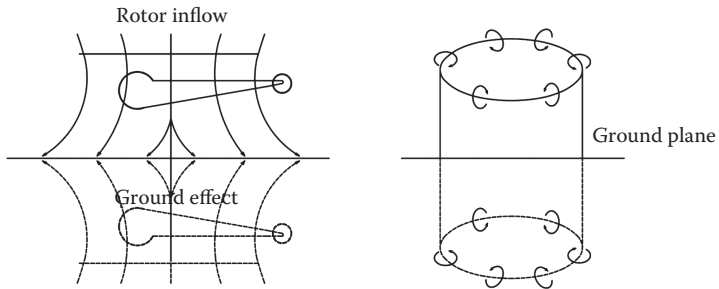
Figure 2.21
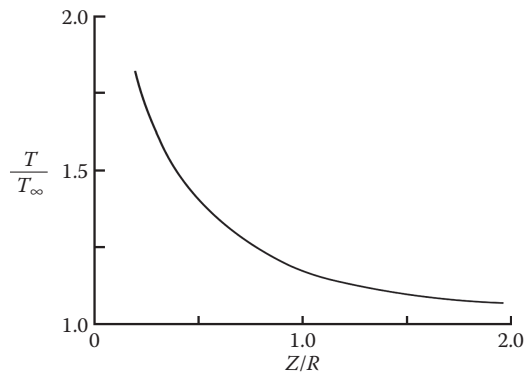Rotor hovering near the ground and method of images.

Figure 2.22
Thrust variation in hover with rotor height from ground.